

## Basic data features and results from a spatially dense seismic array on the San Jacinto fault zone

Yehuda Ben-Zion,<sup>1</sup> Frank L. Vernon,<sup>2</sup> Yaman Ozakin,<sup>1</sup> Dimitri Zigone,<sup>1</sup> Zachary E. Ross,<sup>1</sup> Haoran Meng,<sup>1</sup> Malcolm White,<sup>2</sup> Juan Reyes,<sup>2</sup> Dan Hollis<sup>3</sup> and Mitchell Barklage<sup>3</sup>

<sup>1</sup>Department of Earth Sciences, University of Southern California, Los Angeles, CA 90089-0740, USA. E-mail: [benzion@usc.edu](mailto:benzion@usc.edu)

<sup>2</sup>Scripps Institute of Oceanography, University of California San Diego, La Jolla, CA 92093, USA

<sup>3</sup>Nodal Seismic, Signal Hill, CA 90755, USA

Accepted 2015 March 26. Received 2015 March 25; in original form 2015 February 2

### SUMMARY

We discuss several outstanding aspects of seismograms recorded during >4 weeks by a spatially dense Nodal array, straddling the damage zone of the San Jacinto fault in southern California, and some example results. The waveforms contain numerous spikes and bursts of high-frequency waves (up to the recorded 200 Hz) produced in part by minute failure events in the shallow crust. The high spatial density of the array facilitates the detection of 120 small local earthquakes in a single day, most of which not detected by the surrounding ANZA and regional southern California networks. Beamforming results identify likely ongoing cultural noise sources dominant in the frequency range 1–10 Hz and likely ongoing earthquake sources dominant in the frequency range 20–40 Hz. Matched-field processing and back-projection of seismograms provide alternate event location. The median noise levels during the experiment at different stations, waves generated by Betsy gunshots, and wavefields from nearby earthquakes point consistently to several structural units across the fault. Seismic trapping structure and local sedimentary basin produce localized motion amplification and stronger attenuation than adjacent regions. Cross correlations of high-frequency noise recorded at closely spaced stations provide a structural image of the subsurface material across the fault zone. The high spatial density and broad frequency range of the data can be used for additional high resolution studies of structure and source properties in the shallow crust.

**Key words:** Guided waves; Seismic attenuation; Site effects; Seismic tomography; Wave scattering and diffraction; Wave propagation.

### 1 INTRODUCTION

The properties and dynamics of the heavily damaged material in the top few hundred meters of the crust are understood only in general terms, especially near fault zones, despite their great importance to observed seismic motion, crustal hydrology, subsurface reservoirs and numerous other applications. The low normal stress at shallow depth renders the subsurface material highly susceptible to failure and strongly attenuative, masking properties of deeper structures. Detailed seismological imaging of the very shallow crust can allow velocity and attenuation models to be developed essentially up to the surface, where they may be combined with information derived from geological mapping and boreholes. Monitoring how the subsurface material responds to repeating (e.g. active, tidal, atmospheric-based) sources, along with earthquakes and aseismic deformation, may allow for tracking the evolution of stress. Analysing high-frequency

seismic ‘noise’ can provide insight on near-surface processes and the nature of the sources (including numerous minute local failure events) generating the noise.

To address such issues, and augment larger scale results on source and structural properties within and around the San Jacinto Fault Zone (SJFZ) in southern California, we deployed a spatially dense Nodal array with 1108 vertical (10 Hz) ZLand geophones in ~600 m × 600 m configuration around the Clark branch of the SJFZ (Figs 1 and 2). The array was deployed at the Sage Brush Flat (SGB) site in the complex trifurcation area south of Anza, from 2014 May 7 to 2014 June 13, with a core grid consisting of 20 rows perpendicular to and centred on the Clark fault trace. Each row had 50 sensors at a nominal 10 m interstation spacing and the nominal separation between rows was 30 m. The remaining 108 sensors were deployed as extensions to multiple rows. The array recorded earthquake and noise data continuously at 500 samples s<sup>-1</sup> with useable

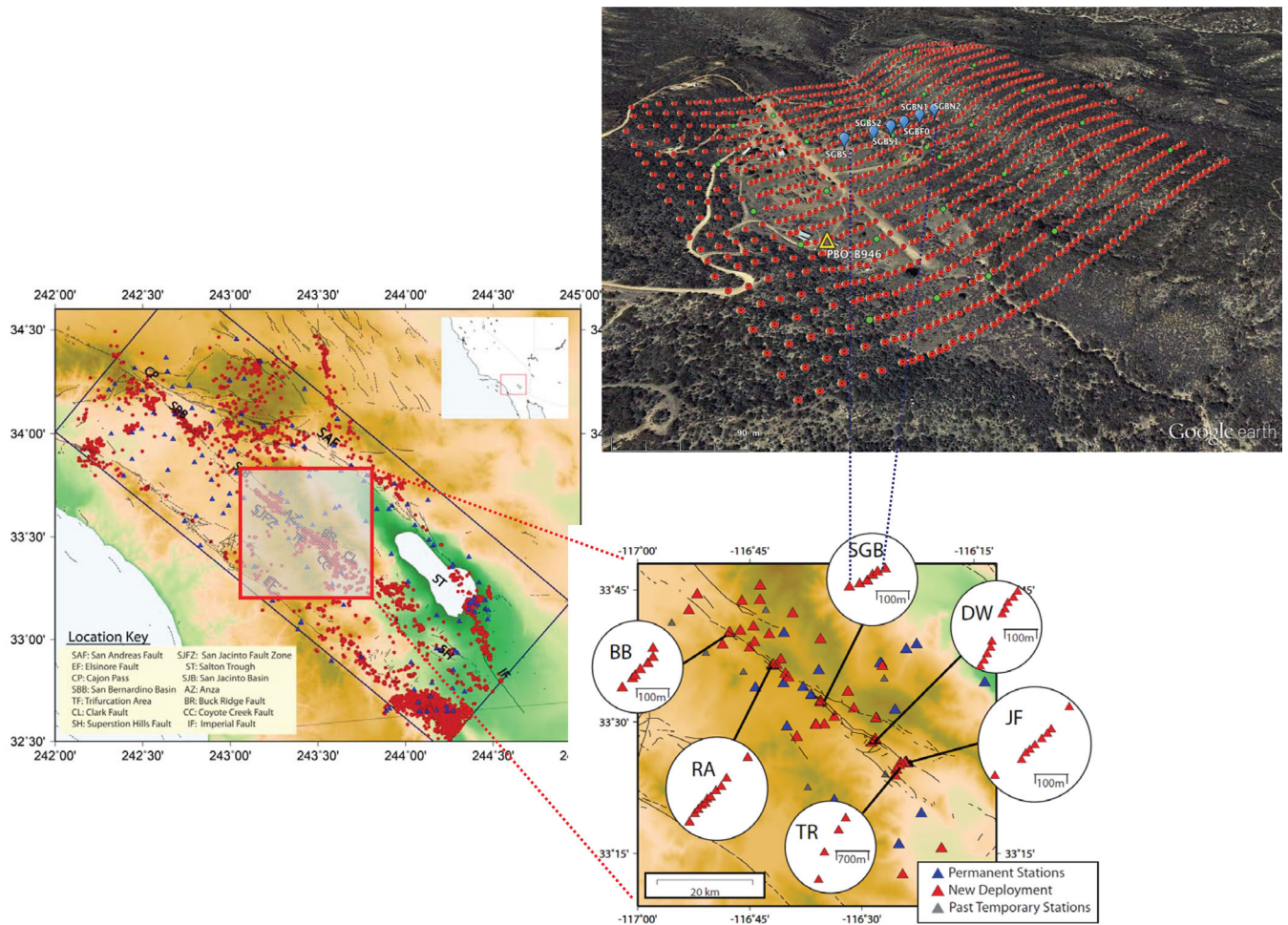


**Figure 1.** Left-hand panel: regional seismic stations (blue triangles) covering scales in the range 1–100 km. Bottom right-hand panel: zoom in showing >70 additional PASSCAL stations around the San Jacinto fault zone (red triangles) and dense across-fault linear arrays. Top right-hand panel: further zoom showing a spatially dense Nodal array with 1108 vertical-component ZLand sensors at site SGB. See text for additional information.

frequencies up to 200 Hz. Additional data were generated by Betsy gunshots at 33 sites of the dense deployment (green circles in Fig. 1, top right-hand panel).

The spatially dense array and other existing stations provide a hierarchical seismic coverage that can be used to study properties and processes around the SJFZ over a broad range of scales. The southern California and ANZA networks cover scales from a few km to over 100 km (Fig. 1, left-hand panel), six dense linear PASSCAL arrays that cross the SJFZ at several locations and additional stand-alone PASSCAL seismometers provide data (from ~2012 to present) over scales ranging from 50 m to several km (Fig. 1 bottom right-hand panel), and the Nodal array covers smaller scales of the fault zone and the very shallow crust (Fig. 1, top right-hand panel). One row of the Nodal array overlaps partially with six three-component PASSCAL seismometers of the linear array SGB (blue symbols in Fig. 1, top right-hand panel), with site SGBS1 also having a seismometer in a ~60 m deep borehole. Some sensors of the spatially dense array are also near a ~100-m-deep PBO borehole site with seismic and strainmeter instruments (yellow triangle in Fig. 1 top right-hand panel).

The data of the regional and PASSCAL seismometers were used in the last few years to obtain earthquake- and noise-based tomographic images with nominal horizontal resolution of 2–3 km over the depth interval 1–15 km (e.g. Allam & Ben-Zion 2012; Zigone

*et al.* 2015), finer-scale information on fault bimaterial interfaces and inner damage zones (order 100 m wide) based on head, trapped, and internally reflected waves (e.g. Yang *et al.* 2014; Qiu *et al.* 2015), characteristics of ground motion generated by  $M_L > 1$  events in the area (Kurzon *et al.* 2014) and source tensor properties of  $M_L > 4$  earthquakes (Ross *et al.* 2015). These studies provided detailed context on structures and processes at seismogenic depths, but they had essentially no resolution in the top few hundred meters of the crust. Analysing structural properties and the behaviour of the shallow crust require high-frequency data at closely spaced stations of the type recorded by the Nodal array. In this paper, we illustrate aspects of the waveforms and results associated with the spatially dense array data. The scope is limited to basic features that demonstrate the potential of the data. More detailed results on various topics will be presented in subsequent papers.

## 2. RESULTS

All the shown results are based on raw data unless indicated otherwise. Fig. 2 provides a location map with main fault traces, stand-alone seismic stations (triangles) and epicentres of earthquakes (circles). The events detected by the ANZA network augmented by temporary PASSCAL stations during the >4 weeks operation

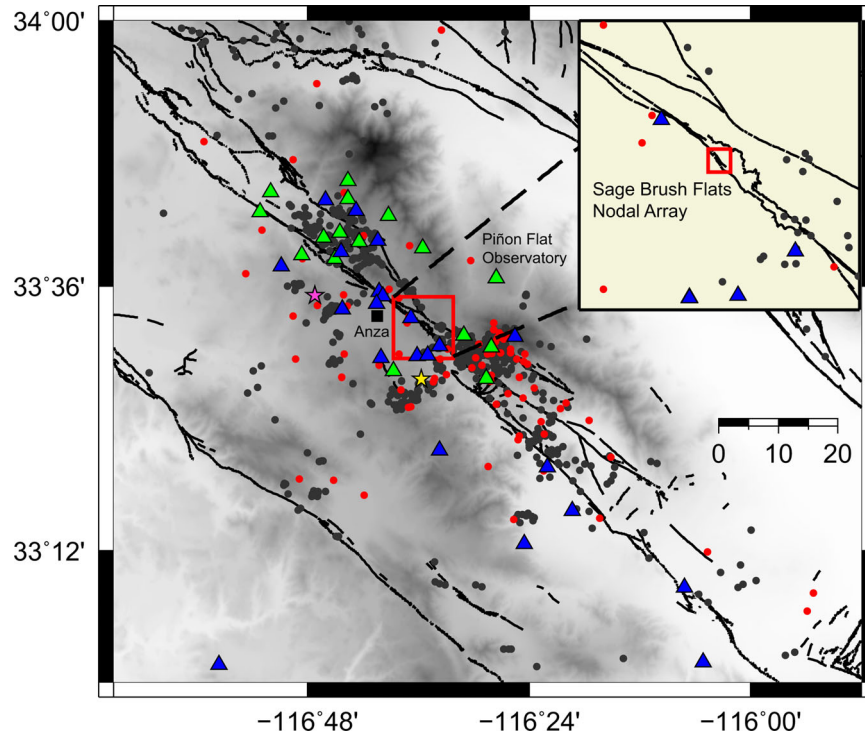


**Figure 2.** Map of seismicity and stations around the spatially dense Nodal array at the Sage Brush Flats site on the SJFZ (red box in the inset). The black circles show locations of events detected during the >4 weeks array operation by stations of the ANZA network (green triangles) and temporary PASSCAL stations (blue triangles). The red circles denote locations of events detected during Julian day 146 using data recorded by the Nodal array (see Fig. 3 for times). The yellow star marks an event located also with matched-field processing and back projection in Fig. 5. Example seismograms from this and the event denoted by the pink star are shown in Figs S1(a) and (b).

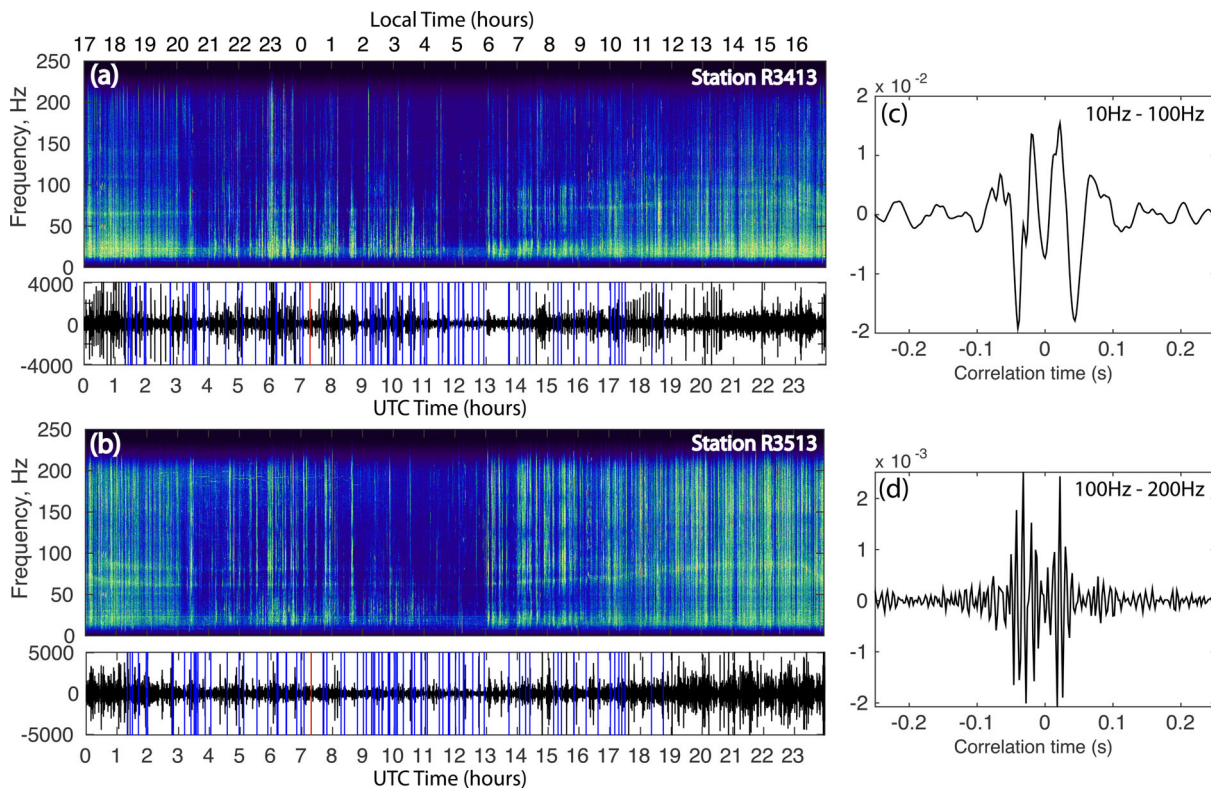


**Figure 3.** (a) and (b) Waveforms and spectrograms recorded at two stations 10 m apart in Julian day 146. The blue vertical lines mark the times of the 120 earthquakes detected using the dense array data (red circles in Fig. 2); the red vertical line corresponds to the event shown as yellow star in Fig. 2 and located also in Fig. 5. (c) and (d) Stacked correlograms at two frequency bands of the waveforms recorded by the two stations in (a) and (b) during the >4 weeks array operation.

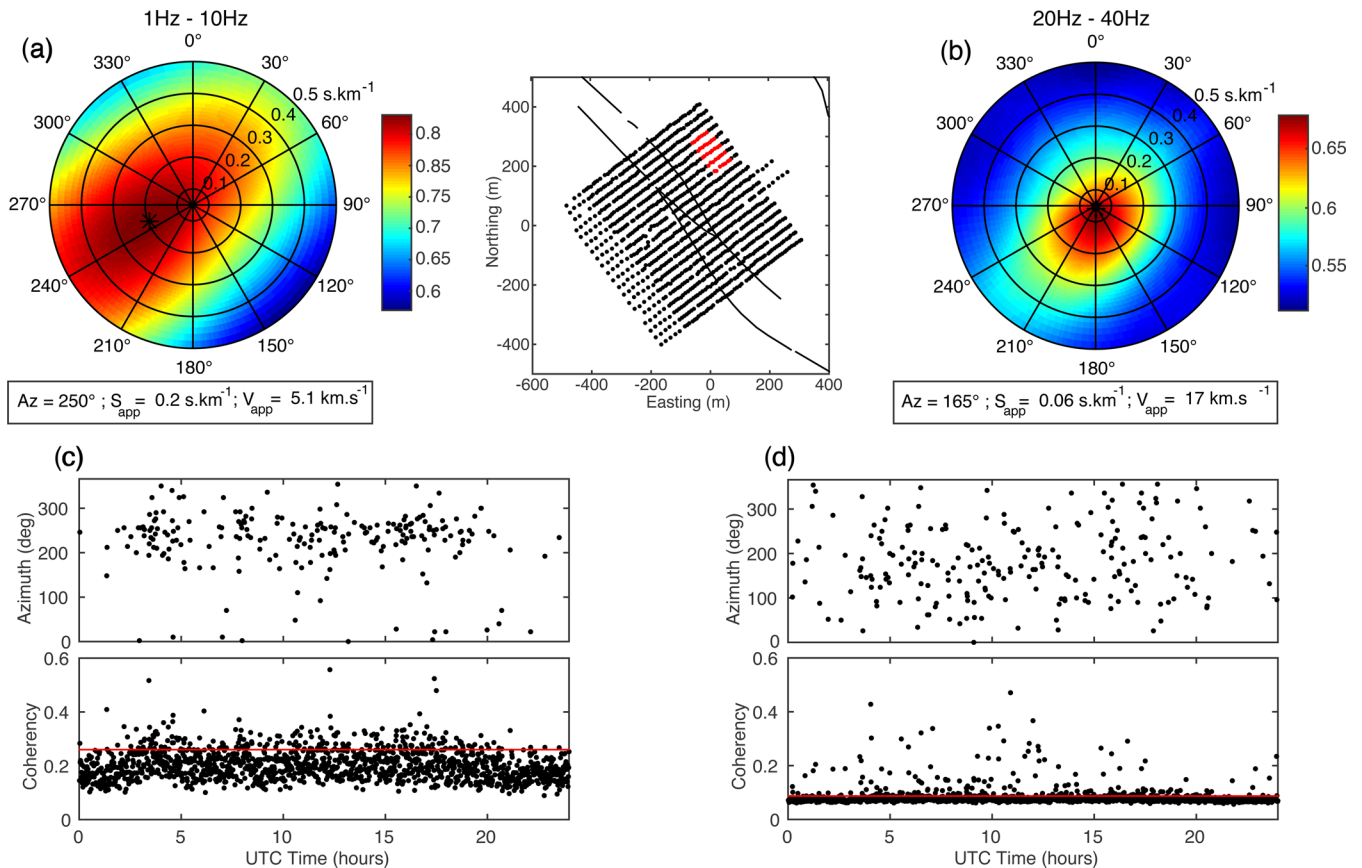


**Figure 4.** Beamforming results for Julian day 146 using the subarray denoted by red dots in the middle top plot of the Nodal array. (a) and (b) Daily slowness-azimuth polar results for 1–10 Hz and 20–40 Hz. The black boxes indicate the azimuth, apparent slowness, and apparent velocity associated with the maxima of the beamforming results (marked by a black star in each polar plot). (c) and (d) Time dependent beamforming results for 1–10 Hz and 20–40 Hz. The bottom panels show coherency values in each 1 min window. The top panels show azimuth values associated with coherency above the thresholds indicated by the horizontal red lines (selected to focus on higher coherency and to have similar number of measurements for both frequency bands).

of the Nodal array are shown by black circles. There are 946 such events with magnitude range  $-0.7 \leq M_L \leq 3.4$  and epicentral distances less than 200 km, and 20 events with magnitude range  $-0.62 \leq M_L \leq 0.66$  and epicentral distances  $\leq 5$  km. For comparison, only eight events with  $0.31 \leq M_L \leq 1.14$  and epicentral distances  $\leq 5$  km were detected in the same time interval by the Southern California Seismic Network. On the other hand, careful examination of the data recorded during Julian day 146 by the spatially dense array provides clear evidence for 120 local quakes in a single day (red circles), of which only 15 and 30 were detected by the regional southern California and ANZA networks, respectively. (Julian day 146 was selected randomly from the days with full network operation and without explosions and field work.) The detection of the additional small quakes is made possible by the high degree of coherency in the waveforms recorded by the spatially dense array. We use this coherency to manually scan 24 hr of the continuous data and identify *P* and when possible also *S* waves across the array. Figs S1(a) and (b) show example *P* waves generated by the events denoted by yellow and pink stars in Fig. 2. Having the times of the events based on the array data, we search for corresponding waves in the nearest ANZA and PASSCAL stations. Although the waves at these stations are barely above the noise level, knowing where they should be allows picking *P* (and sometime also *S*) arrivals for each event in at least three stations. The events are then located (Fig. 2, red circles) using these picks and the Antelope platform.

The median and smallest  $M_L$  values of the events calculated with Antelope are  $-0.29$  and  $-1.58$ , respectively, but these values and the locations are not very accurate since they are based on small data sets.

Inspection of waveforms recorded by the spatially dense array reveals numerous spikes and bursts of high-frequency waves. This is illustrated in Figs 3(a) and (b) using data recorded by two stations in Julian day 146. The results exhibit daily variations with overall quieter night times, but there are sources of high-frequency waves also during the night. Similar features are seen with some spatio-temporal variations at all the array stations as well as in data of the dense linear arrays. Such events are typically lumped (if detected) into the ambient seismic noise. The high frequency content of the events, and the highly attenuative character of the subsurface material, imply that they are generated locally near the stations. Some of the energy bursts may be produced by nearby noise sources (e.g. cultural noise or wind). However, as indicated by the 120 detected events (vertical blue and red lines) and illustrated further below, many sources are located below the surface.

Fig. S2 shows the acceleration power spectral density recorded by one station of the Nodal array on day 146 (with instrument response removed), along with the Peterson High and Low Noise Model and the amplitude response function for the ZLand sensors. The observed spectral levels are halfway between the Peterson Low and High Noise Model curves up to the 10 Hz corner frequency

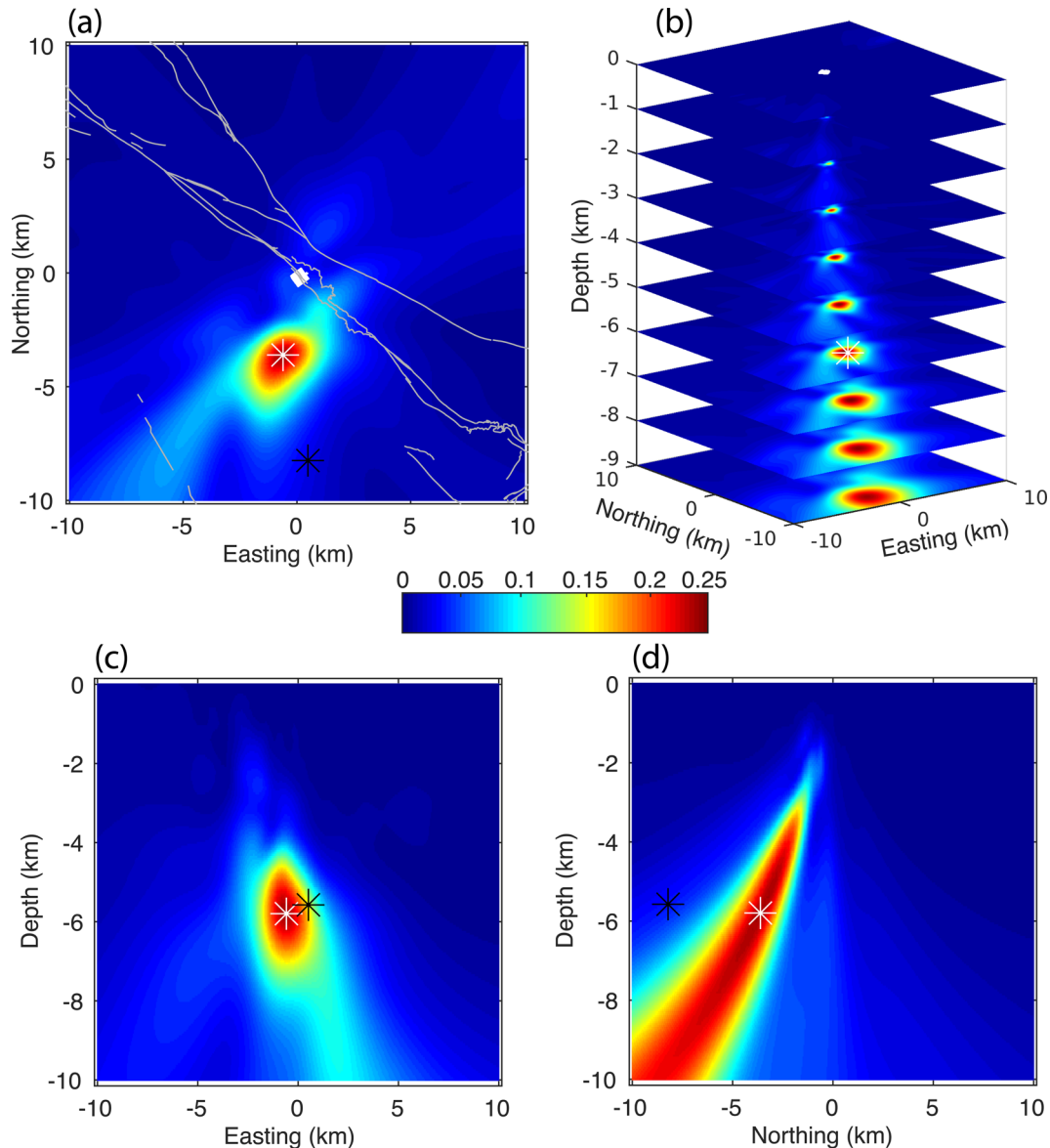


**Figure 5.** Example of locating the small event indicated as yellow star in Fig. 2 using data recorded by 1069 sensors of the Nodal array (white square in panels a and b). The matched-field processing method is used to back-project the seismograms to a finely spaced grid around the array in the frequency domain. The black and white stars indicate, respectively, the original location and best location estimate using the technique. The Bartlett function (colour scale) plotted throughout the grid is observed to focus to a point nearly south of the array at a depth of  $\sim 5.8$  km. (a) Map view with the Nodal array stations used (white square) and fault traces (white lines). (b) A 3-D view of the MFP results. (c) and (d) Depth cross-sections along the east (c) and north (d) directions.

of the ZLand geophone, and continue an overall upward trend until 200 Hz. The time domain and spectral characteristics of the recorded waveforms are quite complex, but they are highly correlated up to 200 Hz at distances of 10–20 m (Figs 3c–d). The degree of correlation decreases with increasing station separation but remains high at frequencies up to 10–15 Hz over the entire Nodal array. These correlation results extend previous small aperture array observations at the nearby Piñon Flat Observatory, which showed *P*-wave coherence in the 10–15 Hz band to at least 250 m (Vernon *et al.* 1998). As demonstrated at the end of this section, the high correlations can be exploited for high-resolution imaging of the very shallow crust.

The spatially dense array provides an opportunity to analyse the frequency dependent characteristics of continuous waveforms using a plane wave beamforming approach in the frequency domain (Fig. 4). The method compares observed phase delays across the

array with those of synthetic sources referred to as replica vector. Noise data are commonly processed in various time windows to accumulate a coherent phase signal (e.g. Gerstoft & Tanimoto 2007; Roux 2009) in the form of a cross-spectral density matrix  $K$ ,

$$K(\omega) = d(\omega)d^*(\omega), \quad (1)$$

where  $d$  is the Fourier transform of the data and the asterisk denotes Hermitian transpose. The replica vector,  $e$ , is generated for a synthetic source at a given azimuth from the array using an assumed apparent velocity  $v$ ,

$$e_i(\theta, v, \omega) = \exp\left(i2\pi \frac{(x_i \sin(\theta) + y_i \cos(\theta))}{v}\right), \quad (2)$$

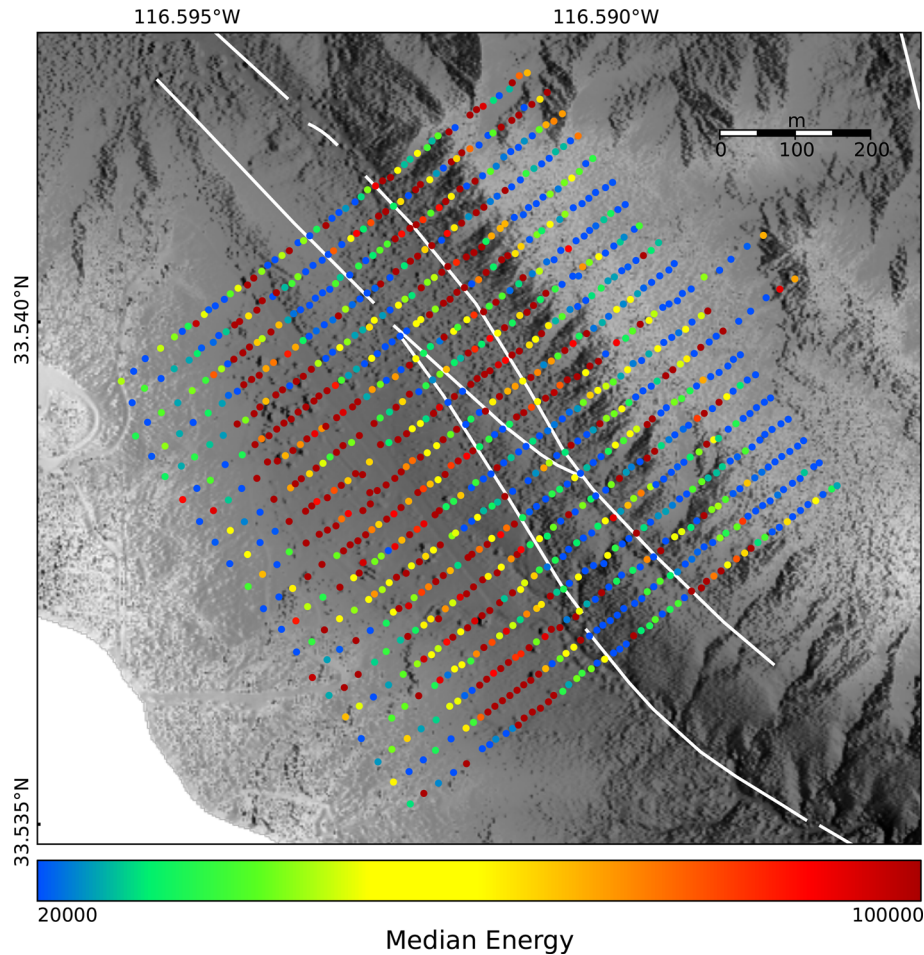


**Figure 6.** Median energy (squared velocities in instrument units) recorded at the array stations (circles) throughout the experiment. The shading shows the local topography and white lines indicate surface traces of the San Jacinto fault. The two zones with amplified motion (reddish colours) are distinguished also in data of subsequent figures.

where  $\theta$  is the azimuth between the synthetic source and sensor  $i$  located at  $(x_i, y_i)$ . A grid search over azimuth and apparent velocity is performed to maximize the linear Bartlett operator,

$$B(\theta, v) = \sum_{\omega} |e^* \cdot K \cdot e|. \quad (3)$$

The values of the Bartlett operator, referred to below as coherency, indicate how well the observed phase delays compare with the theoretical ones for a given set of discrete frequencies  $\omega$ .

We apply the beamforming approach to data in the frequency bands 1–10 Hz and 20–40 Hz recorded during Julian day 146 by a subarray composed of 40 stations of the spatially dense array (red dots in the central panel of Fig. 4). The location and size of the subarray are selected to avoid topographic changes and provide sharp images at both low and high frequency bands. The data are processed using frequency step size of 0.5 Hz and 1 min time windows with no overlap to accumulate coherent phase signals in the  $K$  matrix. The replica vectors are generated every  $1^\circ$  in azimuth and every  $0.1 \text{ km s}^{-1}$  in apparent velocity with a range between 2 and  $20 \text{ km s}^{-1}$ . Fig. 4 shows results for the entire day in the top panels and time dependent beamforming for each 1 minute window in the bottom panels. For 1–10 Hz, there is dominant overall excitation (Fig. 4a) with apparent velocity of  $5.1 \text{ km s}^{-1}$  and azimuth of  $250^\circ$ , pointing to human related structures and machines (house, pumps, trucks, etc.) augmented possibly by ocean/wind sources.

The time dependent analysis (Fig. 4c) illustrates the persistence of these noise sources with ongoing activity from directions with azimuths between  $200^\circ$  and  $300^\circ$ . Note that there is no clear decrease of activity during nighttime (see Fig. 3 for conversion to local time). In contrast, for 20–40 Hz we observe very high overall apparent velocity of  $17 \text{ km s}^{-1}$  and dominant azimuth of  $165^\circ$  (Fig. 4b), indicating sources below the array. The time dependent analysis over this frequency band (Fig. 4d) yields a broad azimuth distribution consistent with many small sources below the array.

The spatially dense array can also be used to locate individual sources of energy. This is illustrated in Fig. 5 for the event indicated in Figs 2 and 3 by the yellow star and vertical red line, respectively. The array-based location is done with a modified version of the matched-field processing (MFP) algorithm of Kuperman & Turek (1997) and Cros *et al.* (2011), and projecting phase delays of the MFP onto a 3-D grid with the linear Bartlett operator. Additional details on this location technique are given in the supplementary material. The results of Fig. 5 are based on data of 1069 stations, using four 0.25 s time windows starting  $\sim 0.25$  s before the  $P$  arrivals and frequency range 10–20 Hz. The back-projection employs a 1-D velocity model extracted from the 3-D tomography results of Zigone *et al.* (2015) for the area. The Bartlett function values (coherency) for this event suggest an epicentral shift of  $\sim 4.5 \text{ km}$  (Fig. 5a) from the location of Fig. 2 and a depth change from  $\sim 5.6$  to  $\sim 5.8 \text{ km}$  (Fig. 5b). We note that the location has large

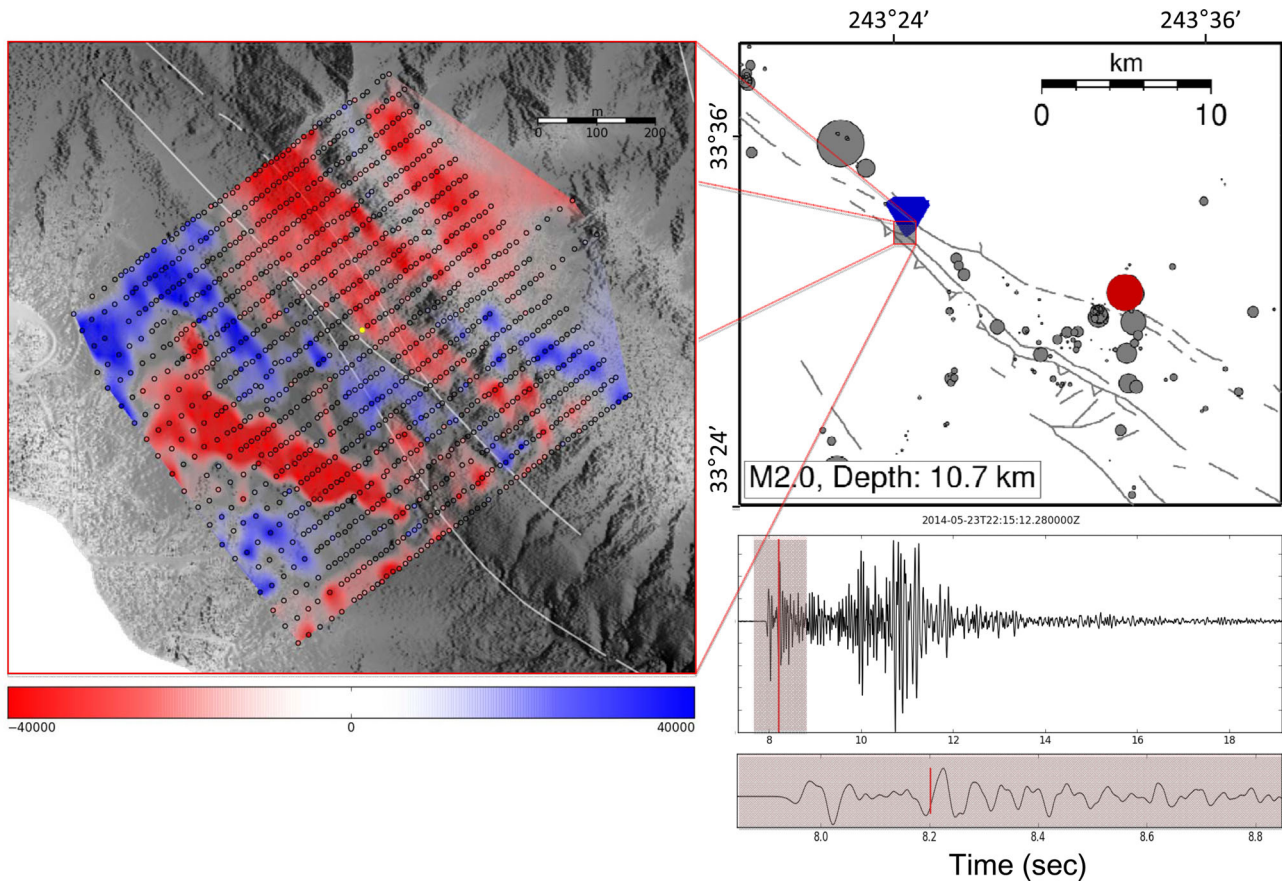


**Figure 7.** A snapshot of ground velocity across the array generated by a nearby earthquake. The colours inside the circles (sensor locations) show observed ground velocities in instrument units at the time of the snapshot. The colours between the circles are obtained by natural neighbour interpolation based on Delaunay triangulation. Surface traces of the fault are marked by white lines and black lines in the inset map. The event and array locations are indicated in the inset map by red circle and blue triangle, respectively. The red vertical line at the bottom right seismogram indicates the used time. The seismogram was recorded at the sensor denoted by a solid yellow circle. See Animations S1 and S2 for additional related data.

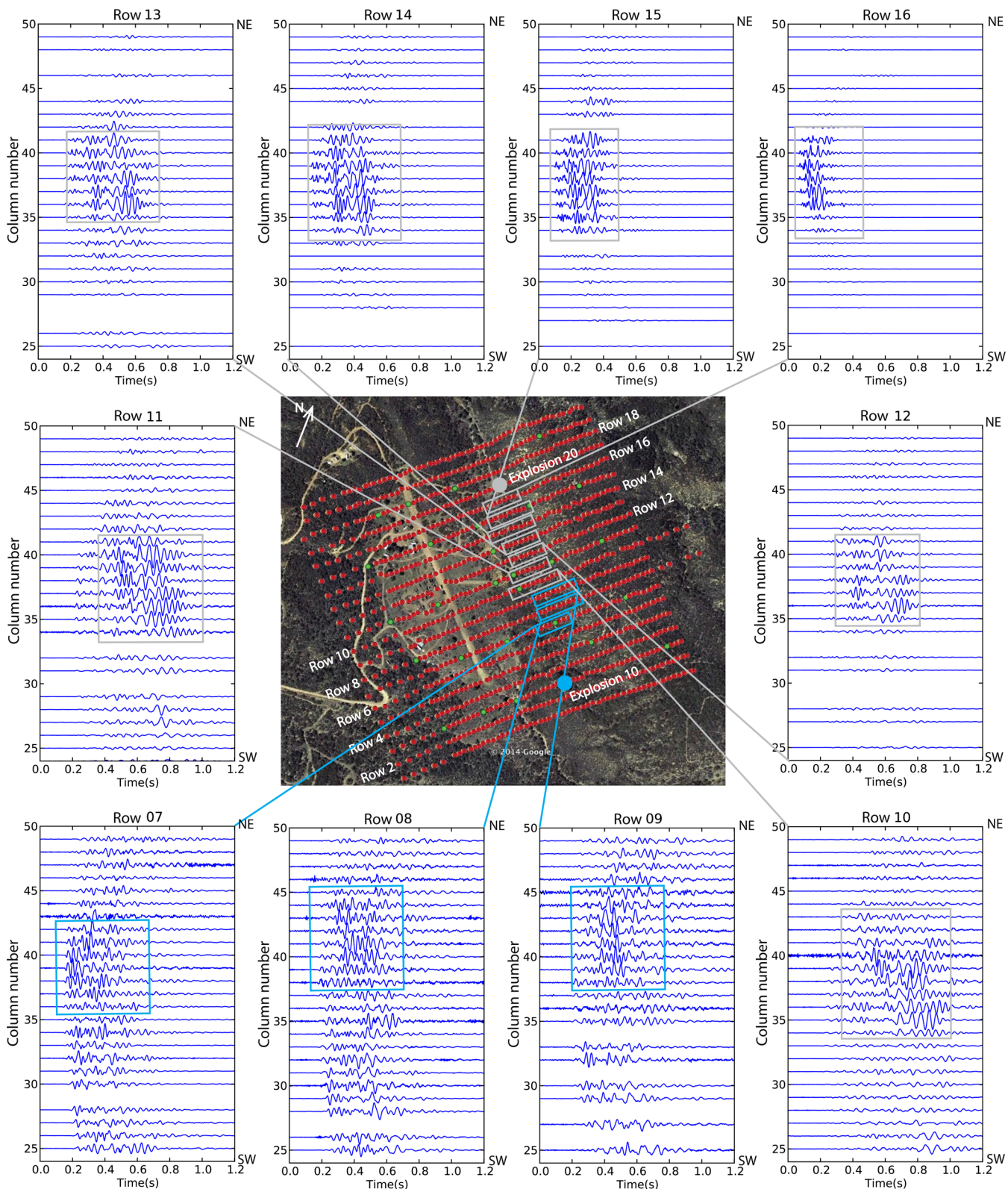
uncertainties stemming from the approximate used velocity model (the corresponding location in Fig. 2 also has large uncertainties). Using a detailed 3-D velocity model (Allam *et al.* 2014; Zigone *et al.* 2015) and possible addition of *S* waves can improve considerably the accuracy of the results.

Fig. 6 displays the median values of the seismic energy (squared amplitudes) recorded across the array during the >4 weeks experiment. The results show two fault-parallel zones that produce motion amplification (reddish colours). The amplifying zone NE of the surface fault trace is associated with a possible seismic trapping structure discussed further below. The other amplifying region SW of the fault is associated with a local sedimentary basin and the landowner's home, water pumps and other machines (cultural noise; Fig. 4 left-hand panel). Similar zones are seen to various degrees by the ground motion generated at the array by earthquakes and additional data. Visual inspection of the evolving wavefields across the array from nearby earthquakes (Animations S1 and S2) suggests waves that are reflected by vertical interfaces in the fault zone structure and additional reflection/refraction/scattering sources. The *P* wavefield from a nearby event is illustrated in Fig. 7 with a snapshot of the ground motion.

Fig. 8 presents composite recordings of waveforms generated by two Betsy gunshots (grey and blue circles). The results show groups of waveforms with large oscillatory late arrivals at subsets of stations enclosed by the grey and blue boxes. These waveform groups have expected characteristics of trapped waves associated

with resonance modes in a vertical low velocity fault zone layer (e.g. Ben-Zion & Aki 1990). Other station-explosion combinations do not show such resonance-type wave groups. Most explosions produce circular wave fronts that deteriorate during propagation with increasing scattering (Animation S3). In contrast, explosions 20 and 10 produce wave packets that propagate along the tabular trapping zone (Animation S4), with scattered waves around the trapping structure and some motion amplification in the local sedimentary basin to the SE. The stations recording trapped waves are within the damage zone NE of the fault trace producing amplified ground motion and wave reflections (Figs 6 and 7). As shown next and in supplementary Fig. S3, the same zone has low wave velocities and is also strongly attenuative compared to adjacent regions.

Fig. 9 presents group velocities of Rayleigh waves at 50 Hz across the fault, constructed from cross correlations of noise recorded by row 13 of the array. The results are based on daily correlation functions between the 55 stations of row 13 using a modified version of the pre-processing procedure of Zigone *et al.* (2015). This involves earthquakes removal, whitening between 30 and 60 Hz and amplitude clipping at three times the standard deviation on 15 min time windows. The daily correlation functions are stacked for the duration of the experiment; the stacked correlations exhibit coherent Rayleigh waves that travel between station pairs (e.g. Figs 3c–d). After rejecting paths without sufficient signal to noise ratios, the Rayleigh group velocity measurements at 50 Hz are inverted with



**Figure 8.** Collection of waveforms generated by two explosions marked by grey and blue circles and recorded by sets of sensors enclosed in corresponding grey and blue rectangles. The waveform groups enclosed by boxes are fault zone trapped waves. See Animations S3 and S4 for additional related data.

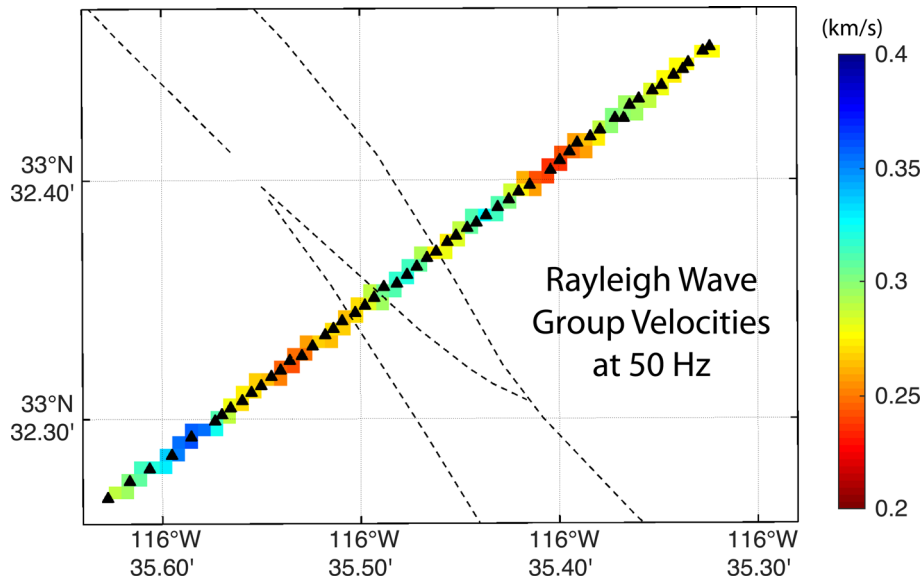


**Figure 9.** Rayleigh wave group velocities (colour scale) at 50 Hz along row 13 of the array. The black triangles are sensors and dashed lines indicate surface traces of the fault. Note the zones with significant velocity reduction.

the procedure of Barmin *et al.* (2001) onto a 10-m-grid size. The obtained values are approximate, since topographic changes are not accounted for, but they are overall consistent with the previously discussed results. More accurate tomographic images will be provided by later studies.

### 3 DISCUSSION

The shallow crust strongly affects various aspects of observed ground motion, given its very low seismic velocities and attenuation coefficients, and it plays important roles in numerous engineering, resource exploration and other applications. The seismic structure in the top few hundred meters is generally ‘invisible’ to typical tomographic imaging and is known in detail only at isolated borehole locations and sites of extensive commercial surveys. In this paper, we outline basic features of seismic records from a spatially dense Nodal array on the SJFZ generated by earthquakes, ambient noise and small explosions. We note that the distinction between small earthquakes and ambient noise becomes obscure (Fig. 3) in high-frequency data of the type used in this work. The short (10–30 m) interstation spacing and relatively high recorded frequencies provide unique opportunities for studying the properties and dynamics of the shallow crust. The hierarchical seismic coverage around the array (Fig. 1) allows the results to be combined with larger scale fault zone and regional models, as well as with borehole and geological information.

The observations of Figs 2–4 indicate that the subsurface material sustains multitudinous small failure events and is far more dynamic than is generally assumed. The ongoing occurrence of such events is expected to produce collectively small temporal changes of seismic velocities in the shallow crust (e.g. Richter *et al.* 2014; Hillers *et al.* 2015). Laboratory experiments and seismic observations indicate that post-failure material healing (regaining of elastic moduli) follows a  $\log(t)$  functional form, with substantial recovery on timescales of hours even at conditions corresponding to very shallow depth (e.g. Dieterich & Kilgore 1996; Johnson & Jia 2005; Wu *et al.* 2009). However, the persisting very low velocities and strong attenuation of the subsurface material imply incomplete or

‘frustrated’ healing involving ongoing failures. This is consistent with the simple event detection analysis done in this work. A manual inspection of the spatially dense data reveals 120 small quakes in a single day (Figs 2 and 3). Using these events as templates and/or combining matched-field, migration and other techniques (Ross *et al.*, in preparation) can lead to detection of many additional smaller failure events.

Our example results demonstrate that the highly dense array data can be used to track the coherency of waves over various distances as a function of location and frequency bands (Figs 3, S2, 4, 7–9), observe structural properties producing motion amplification, resonance modes and other wave characteristics (Figs 6–9 and Animations S1–S4), analyse attenuation of waves in the subsurface material (Fig. S3) and improve the detection and location of energy sources (Figs 2–5). Systematic detection and location of the tiny subsurface quakes is highly challenging given their small size and vast number. A useful strategy may combine pseudo-probabilities of various detectors with matched-field and migration techniques (e.g. Corciulo *et al.* 2012; Ross & Ben-Zion 2014; Ross *et al.*, in preparation). A catalogue with space–time–size attributes of the minute failure events can provide, in conjunction with monitoring temporal property changes, fundamental information on the effective rheology of the subsurface material, evolving stress in the shallow crust, and spatial heterogeneities of the loadings and material properties.

The close spacing and large number of instruments in the Nodal array present many additional research possibilities. These include eikonal and Helmholtz tomographies (e.g. Lin *et al.* 2013; Mordret *et al.* 2013), reconstruction of focal spots from time-reversed wave fronts for wave speed estimates (e.g. Catheline *et al.* 2008; Hillers *et al.* 2014), monitoring changes of seismic properties over various timescales (e.g. Richter *et al.* 2014; Hillers *et al.* 2015), clarifying the contributions of far-field, regional and local sources to the ambient seismic noise (e.g. Hillers & Ben-Zion 2011; Zhan *et al.* 2014), examining signatures in the wavefield that might indicate rock damage in source volumes (e.g. Castro & Ben-Zion 2013; Ross *et al.* 2015), and conducting multiple beamforming with various subarrays to clarify wave propagation properties between the arrays (e.g. Boué *et al.* 2013). The existence of boreholes in the location of the spatially dense array (Fig. 1) provide further opportunities for

detailed imaging of the subsurface structure including nonlinear wave propagation effects (e.g. Pasqualini *et al.* 2007; Wu *et al.* 2010) and anisotropy of seismic velocity and attenuation (e.g. Hauksson *et al.* 1987; Liu *et al.* 2005). Work on a number of these topics is underway.

## ACKNOWLEDGEMENTS

We are grateful to Bud Wellman for allowing us to deploy the instruments on his property. Geoff Davis, Jon Meyer, Pieter-Ewald Share, Xin Liu, Cooper Harris, Maxwell Dalquist, Hongrui Qiu, Valerie Sahakian and Nicholas Mancinelli helped with the field work. Rob Clayton and Paul Davis kindly provided the Betsy gun. The paper benefitted from useful comments by Philippe Roux, Gregor Hillers, two anonymous referees and editor Jeannot Trampert. The study was supported by the National Science Foundation grants EAR-0908903 (USC) and EAR-0908042 (UCSD).

## REFERENCES

- Allam, A.A. & Ben-Zion, Y., 2012. Seismic velocity structures in the Southern California plate-boundary environment from double-difference tomography, *Geophys. J. Int.*, **190**, 1181–1196.
- Allam, A.A., Ben-Zion, Y., Kurzon, I. & Vernon, F.L., 2014. Seismic velocity structure in the Hot Springs and Trifurcation Areas of the San Jacinto Fault Zone, California, from double-difference tomography, *Geophys. J. Int.*, **198**, 978–999.
- Barmin, M., Ritzwoller, M. & Levshin, A., 2001. A fast and reliable method for surface wave tomography, *Pure appl. Geophys.*, **158**(8), 1351–1375.
- Ben-Zion, Y. & Aki, K., 1990. Seismic radiation from an SH line source in a laterally heterogeneous planar fault zone, *Bull. seism. Soc. Am.*, **80**, 971–994.
- Boué, P., Roux, P.E., Campillo, M. & De Caqueray, B., 2013. Double beam-forming processing in a seismic prospecting context, *Geophysics*, **78**(3), V101–V108.
- Castro, R.R. & Ben-Zion, Y., 2013. Potential signatures of damage-related radiation from aftershocks of the 4 April 2010 (Mw 7.2) El Mayor-Cuapah Earthquake, Baja California, México, *Bull. seism. Soc. Am.*, **103**, 1130–1140.
- Catheline, S., Benech, N., Brum, J. & Negreira, C., 2008. Time reversal of elastic waves in soft solids, *Phys. Rev. Lett.*, **100**, 064301, doi:10.1103/PhysRevLett.100.064301.
- Corciulo, M., Roux, P., Campillo, M., Dubucq, D. & Kuperman, W.A., 2012. Multiscale matched-field processing for noise-source localization in exploration geophysics, *Geophysics*, **77**, 33–41.
- Cros, E., Roux, P., Vandemeulebrouck, J. & Kedar, S., 2011. Locating hydrothermal acoustic sources at Old Faithful Geyser using matched field processing, *Geophys. J. Int.*, **187**, 385–393.
- Dieterich, J.H. & Kilgore, B.D., 1996. Imaging surface contacts: power law contact distributions and contact stresses in quarts, calcite, glass, and acrylic plastic, *Tectonophysics*, **256**, 219–239.
- Gerstoft, P. & Tanimoto, T., 2007. A year of microseisms in Southern California, *Geophys. Res. Lett.*, **34**, L20304, doi:10.1029/2007GL031091.
- Hauksson, E., Teng, T.-L. & Henyey, T.L., 1987. Results from a 1500 M deep, three-level downhole seismometer array: site response, low Q values, and  $f_{max}$ , *Bull. seism. Soc. Am.*, **77**, 1883–1904.
- Hillers, G. & Ben-Zion, Y., 2011. Seasonal variations of observed noise amplitudes at 2–18 Hz in southern California, *Geophys. J. Int.*, **184**, 860–868.
- Hillers, G., Campillo, M., Ben-Zion, Y. & Roux, P., 2014. Seismic fault zone trapped noise, *J. geophys. Res.*, **119**, doi:10.1002/2014JB011217.
- Hillers, G., Retailliau, L., Campillo, M., Inbal, A., Ampuero, J.-P. & Nishimura, T., 2015. In-situ observations of velocity changes in response to tidal deformation from analysis of the high-frequency ambient wave field, *J. geophys. Res.*, **120**, 210–255.
- Johnson, P.A. & Jia, X., 2005. Nonlinear dynamics, granular media and dynamic earthquake triggering, *Nature*, **473**, 871–874.
- Kuperman, W.A. & Turek, G., 1997. Matched field acoustics. *Mech. Syst. Signal Pr.*, **11**, 141–148.
- Kurzon, I., Vernon, F.L., Ben-Zion, Y. & Atkinson, G., 2014. Ground motion prediction equations in the San Jacinto Fault Zone—significant effects of rupture directivity and fault zone amplification, *Pure appl. Geophys.*, **171**, 3045–3081.
- Lin, F.-C., Li, D., Clayton, R. & Hollis, D., 2013. High-resolution shallow crustal structure in Long Beach, California: application of ambient noise tomography on a dense seismic array, *Geophysics*, **78**(4), Q45–Q56.
- Liu, Y., Teng, T.L. & Ben-Zion, Y., 2005. Near-surface seismic anisotropy, attenuation and dispersion in the aftershock region of the 1999 Chi-Chi earthquake, *Geophys. J. Int.*, **160**(2), 695–706.
- Mordret, A., Shapiro, N.M., Singh, S., Roux, P., Montagner, J.-P. & Barkved, O.I., 2013. Azimuthal anisotropy at Valhall: the Helmholtz equation approach, *Geophys. Res. Lett.*, **40**, 1–6.
- Pasqualini, D., Heitmann, K., TenCate, J., Habib, S., Higdon, D. & Johnson, P., 2007. Nonequilibrium and nonlinear dynamics in Berea and Fontainebleau sandstones: low-strain regime, *J. geophys. Res.*, **112**, B01204, doi:10.1029/2006JB004264.
- Qiu, H., Ben-Zion, Y., Ross, Z.E., Share, P.-E. & Vernon, F., 2015. Internal structure of the San Jacinto fault zone at Jackass Flat from earthquake data recorded by a dense linear array, Abstract of the annual SSA meeting.
- Richter, T., Sens-Schönfelder, C., Kind, R. & Asch, G., 2014. Comprehensive observation and modeling of earthquake and temperature related seismic velocity changes in northern Chile with passive image interferometry, *J. geophys. Res.*, **119**, doi:10.1002/2013JB010695.
- Ross, Z.E. & Ben-Zion, Y., 2014. An earthquake detection algorithm with pseudo probabilities of multiple indicators. *Geophys. J. Int.*, **197**, 458–463.
- Ross, Z.E., Ben-Zion, Y. & Zhu, L., 2015. Isotropic source terms of San Jacinto fault zone earthquakes based on waveform inversions with a generalized CAP method, *Geophys. J. Int.*, **200**, 1269–1280.
- Roux, P., 2009. Passive seismic imaging with direct ambient noise: application to surface waves and the San Andreas fault in Parkfield, CA, *Geophys. J. Int.*, **179**, 367–373.
- Vernon, F.L., Pavlis, G., Owens, T., McNamara, D. & Anderson, P., 1998. Near surface scattering effects observed with a high-frequency phased array at Pinyon Flats, California. *Bull. seism. Soc. Amer.*, **88**, 1548–1560.
- Wu, C.Z. & Peng, Z. & Ben-Zion, Y., 2009. Non-linearity and temporal changes of fault zone site response associated with strong ground motion, *Geophys. J. Int.*, **176**, 265–278.
- Wu, C.Z., Peng, Z. & Ben-Zion, Y., 2010. Refined thresholds for nonlinear ground motion and temporal changes of site response associated with medium size earthquakes, *Geophys. J. Int.*, **182**, 1567–1576.
- Yang, H., Li, Z., Peng, Z., Ben-Zion, Y. & Vernon, F., 2014. Low velocity zones along the San Jacinto Fault, Southern California, from body waves recorded in dense linear arrays, *J. geophys. Res.*, **119**, 8976–8990.
- Zhan, Z., Tsai, V.C., Jackson, J.M. & Helmlberger, D.V., 2014. Ambient noise correlation on the Amery Ice Shelf, East Antarctica, *Geophys. J. Int.*, **196**, 1796–1802.
- Zigone, D., Ben-Zion, Y., Campillo, M. & Roux, P., 2015. Seismic tomography of the Southern California plate boundary region from noise-based Rayleigh and Love Waves, *Pure appl. Geophys.*, **172**, 1002–1032.

## SUPPORTING INFORMATION

Additional Supporting Information may be found in the online version of this paper:

**Figure S1.** Example seismograms generated by the events marked in Fig. 2 by the (a) yellow star and (b) pink star. The data are recorded by sensors of the spatially dense array along the blue lines in the inset maps. The *P* waves are coherent across the stations and

have very high apparent velocity (no moveout). Identifying such  $P$  waves in sparsely spaced stations is considerably more difficult.

**Figure S2.** (a) Typical ground acceleration power spectral density for the Nodal array (station R2001 and data of Julian day 146). The time-series for the DPZ channel is given in the top plot. The bottom plot shows power spectrum with instrument response removed (thick blue line), 95 per cent uncertainty (thin blue lines), and Peterson High and Low Noise Model values (red and green lines, respectively). (b) Normalized velocity amplitude response of the 10 Hz Zland seismograph, with a flat response to ground velocity from the 10 Hz geophone corner frequency to 200 Hz where the anti-aliasing FIR filters take effect.

**Figure S3.** Left-hand panel: waveforms generated by two Betsy gun explosions (blue circles in insets) recorded in nearby zones (blue lines in insets). Each seismogram is normalized by its peak value and aligned on the pulse centre. Right-hand panel:  $\log(\text{amplitude})$  and dominant frequency of the waves at different sensors. The top plots with stronger attenuation correspond to the low velocity zone producing amplified motion, wave reflections and trapped waves (Figs 6–9). The dashed lines at the bottom left plot indicate  $P$  and Rayleigh waves propagating, respectively, at velocities of about 450 and 265  $\text{m s}^{-1}$ .

**Animation S1.** Space–time variations of  $P$  waves across the array generated by a nearby earthquake slightly to the NW of the array. The animation shows ground velocities with 10 frames per second. The colours inside the circles (sensor locations) denote observed

ground velocities (in instrument units) and the colours between the circles are obtained by natural neighbour interpolation based on Delaunay triangulation. The shading shows the local topography. Surface traces of the San Jacinto fault are marked by white lines in the main figure and black lines in the inset map. The event and array locations are indicated in the inset map by red circle and blue triangle, respectively. The  $P$  waveform at the bottom was recorded by the sensor indicated by the solid yellow circle.

**Animation S2.** Same as Animation S1 for a nearby earthquake slightly to the SE of the array.

**Animation S3.** Waves generated by explosion 21 (star) in a zone adjacent to the trapping structure. The animation shows ground velocities with 50 frames per second. Each frame is normalized separately to enhance the wave amplitudes at later times. The waveform at the bottom was recorded by the sensor indicated by the solid yellow circle.

**Animation S4.** Same as Animation S3 for waves generated by explosion 21 in the trapping structure. Note the existence of trapped waves in the seismogram at the bottom.

(<http://gji.oxfordjournals.org/lookup/suppl/doi:10.1093/gji/ggv142/-/DC1>).

Please note: Oxford University Press is not responsible for the content or functionality of any supporting materials supplied by the authors. Any queries (other than missing material) should be directed to the corresponding author for the paper.